Microsystem Technologies
https://doi.org/10.1007/s00542-022-05328-2

TECHNICAL PAPER

Analysis of selective bonding processes using reactive multi-layers for system integration on LTCC based SiPs

A. Yuile[1] · A. Schulz[2] · J. Müller[2] · S. Wiese[1]

Received: 25 May 2021 / Accepted: 31 May 2022

Abstract
This paper discusses the use of reactive multi-layers for selective assembly of ICs (Integrated Circuits) in an LTCC (Low Temperature Co-fired Ceramics) based SiP (System-in-Package). To understand the requirements for the use of self-propagating reactive multilayers in die bonding, CFD (Computational Fluid Dynamics) simulations have been carried out to simulate the die bonding process of a silicon chip onto a ceramic LTCC substrate. Reactive foils of 40 and 80 µm thicknesses and a simulated reaction propagation speed of 1 m/s were studied and used to melt a solder preform underneath a silicon chip. The results of the CFD simulations were analysed, particularly with respect to temperature and liquid fraction contours, as well as time–temperature histories obtained from temperature probes which were included in the model, such as to approximate the real behaviour of Pt-100 temperature probes, when a real bonding process is being tracked. The CFD method, in this instance realised with ANSYS Fluent software, can track the melting and solidification of the solder as well as model the influence of latent heat, which is crucial to ascertaining the true evolution of the bonding process.

1 Introduction

SiP brings together different chips into a single form factor package and this approach is gaining in popularity due to offering more functionality, as well as improved miniaturisation and reliability (Zeng et al. 2018). LTCC technology is the preferred platform for high-performance SiP (Park et al. 2006) and it provides a number of advantages, when it comes to heterogeneous system integration tasks that include specific circuitry or components. These include high frequency or millimetre wave circuits (Lee and Park 2016; Seok et al. 2014; Wilde 2009), Ball Grid Array technologies (He et al. 2014; Kangasvieri et al. 2008; Li et al. 2018), fluidic/microfluidic structures for medical applications (Ciobanu et al. 2015), power LED packaging (Lee et al. 2013), RF-antennas (Aliouane et al. 2011), fibre optical applications (Wörhoff et al. 2016) and 3-D microchannel cooling systems (Jia et al. 2012).

In addition to its multilateral functionality LTCC packages provide a high reliability (Golonka et al. 2011; Wilde 2009) with regard to a superior thermal mechanical integrity, very good chemical resistance (Bittner and Schmid 2009; Fournier 2010; Thelemann et al. 2007) and high level of hermiticity (Fournier 2010; Wilde 2009). The need for appropriate reliability characteristics also makes LTCC packages favourable for automotive applications (Golonka et al. 2011). Taking its high cost factor into account, LTCC technology is particularly suited to specific high performance applications, such as military, space, biomedical, and millimetre wave communication (Golonka et al. 2011).

Cost intensive technological processes, that are usually not considered in standard technologies, might still be an option for some of the LTCC technological pathways in manufacturing complex heterogeneous microsystems. Hence, low temperature bonding techniques, using targeted, localised temperature bonding strategies are being increasingly pursued to minimise the damaging effects of mechanical stress on various components.

A viable method of achieving this is using nanoscale reactive multi-layers, that consist of two alternating layers of reagents, in order to deploy a local heat source on a

✉ A. Yuile
adam.yuile@uni-saarland.de

[1] Chair of Microintegration and Reliability, Saarland University, Campus C6.3, 66123 Saarbrücken, Germany

[2] Department of Electronics Technology, Faculty of Electrical and Computer Engineering, TU Ilmenau, 98693 Ilmenau, Germany

Published online: 01 August 2022

targeted area. This is particularly beneficial for integrating disparate components, both with regards to their function and thermal behaviour, and because the further miniaturisation of interconnects is increasing the challenge to minimise temperature exposure during manufacturing.

These reactive multilayer thin films consist of a well-defined energetic material, heterogeneous in its structure and of stored chemical energy (Adams 2015). The reactive multilayers consist of thin layers of reactants, alternating between layers of different metastable solids, whose thickness varies in the range 10–300 nm (Sen et al. 2017), combining to a total thickness in the range of ~ 0.1–300 µm (Adams 2015). The constituents used are typically chosen based on their predisposition to make a reaction and to generate heat. The most basic method of obtaining such a multilayer system is through layer-by-layer magnetron assisted deposition (Rogachev and Mukasyan 2010). Vacuum deposition and more cost-effective mechanical methods can be used as alternatives (Rogachev 2008).

If the reactants are sufficiently heated, then they begin to spontaneously intermix on the atomic scale, as per Fig. 1 from left to right, releasing heat in the process (Raić et al. 2011) and the reactive foils are able to maintain a self-propagating homogeneous reaction of their constituents (Adams 2015), meanwhile exothermically releasing heat, for the purpose of melting surrounding solder to establish a connection or bond. The reaction wave can be initiated through means of short-time local heating of multilayer nanofilms by an electric spark or laser pulse (Rogachev and Mukasyan 2010), whereafter the reaction wave doesn't require external sources of heat to maintain propagation, i.e. the reaction then self-propagates.

While the deposition of reactive multilayers is well established on silicon substrates (Braeuer et al. 2012) it is more challenging to build up a nanolayer structure on an LTCC substrate. The main obstacle is the intrinsic roughness of LTCC substrates, which is in the range of 0.4–1 µm (Bittner et al. 2010; Jantunen et al. 2003; Matters-Kammerer et al. 2006). A successful deposition of reactive multilayers on LTCC substrates was reported by (Grieseler et al. 2012). The LTCC substrates were covered by a brazeable silver system to overcome the problem of surface roughness. Thereafter an additional 5 µm SAC solder was deposited to further adapt the rough LTCC substrate to the reactive nanolayer pile.

The intention of the current solution is, to deposit the reactive multilayer on a well electrically isolated surface. Therefore, in order to adapt the nanolayer pile to the rough surface of the LTCC substrate, a dielectric layer is printed on the substrate, as per Fig. 2, with a cross section of the reactive multilayer on a LTCC substrate being shown in Fig. 3. The configuration in Fig. 2 required a so called tape-on-substrate (TOS) process, (Patterson et al. 1989), and adding a screen-printed dielectric paste to the fired substrate, which involves a brief drying step and an additional 2-h sintering process to realise.

2 CFD model

A three-dimensional (3-D) CFD shoebox model was created in order to assess multi-layer reactive foil usage in joining processes, as initially developed in (Yuile and Wiese 2020). This model was created in ANSYS Fluent 2021 R2 and comprised various layers, namely the chip, solder, reactive foil, substrate, three temperature probes and the surrounding environment, with each feature highlighted in Fig. 4. The shoebox was both 4 mm in length and breadth respectively, with the following layer thicknesses, 400 µm for the Si chip, solder 200 µm and an LTCC thickness of 570 µm. The total reactive foil thickness was 40 µm or 80 µm for the two cases which were studied. A total reactive foil thickness of 80 µm corresponds to the upper limit of commercially available Ni/Al

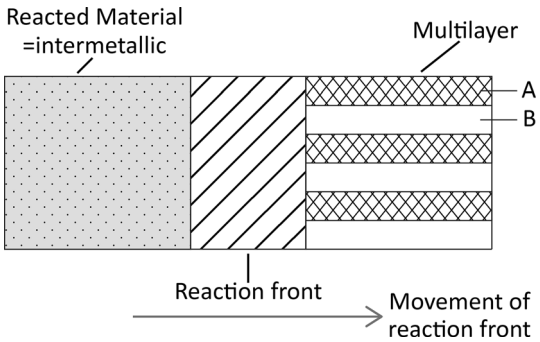

Fig. 1 Schematic showing the progression of the reactive multilayer system

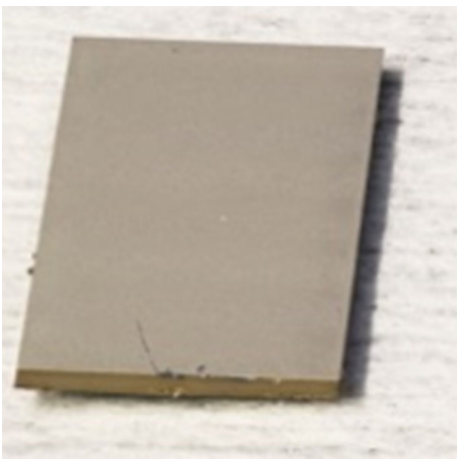

Fig. 2 Deposition of dielectric layer on LTCC

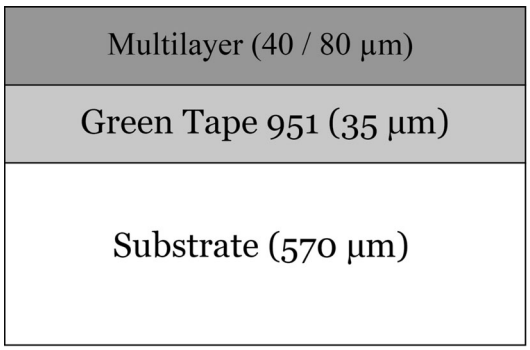

Fig. 3 Cross-section schematic of reactive multilayer on LTCC substrate with 35 µm isolation layer as modelled in CFD

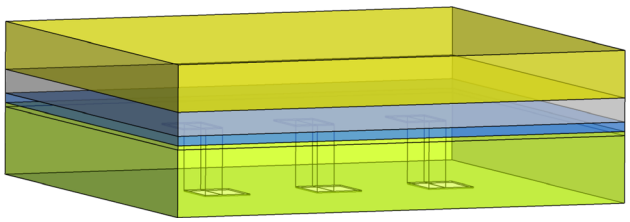

Fig. 4 Close-up of shoebox model layers (semi-transparent) from top to bottom (Yellow = Si, Grey = Solder, Blue = Reactive foil, Green = Green tape ceramic structures)

reactive foils used for bonding silicon with solder (Adams 2015).

A structured mesh, as per Fig. 5, using the same meshing approach as in (Yuile et al. 2022), of 5,262,504 elements for the 40 µm rms (reactive multilayer system) mesh and a comparable 5,376,420 elements for the 80 µm rms mesh was used, with hexagonal elements of 10 µm edge length in the z-direction and 100 µm edge length in both the x- and y-directions respectively.

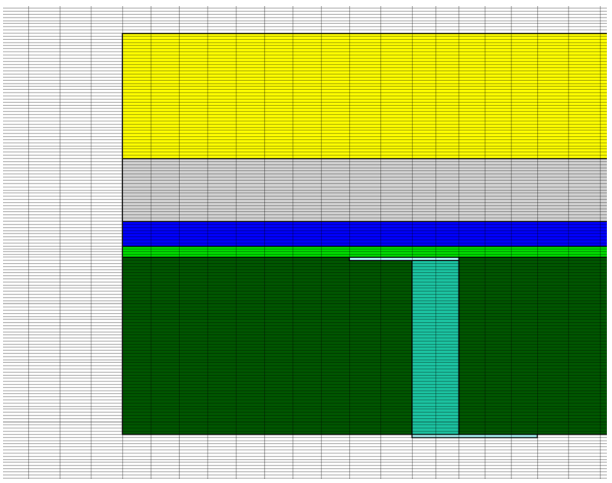

Fig. 5 Close-up of mesh and first temperature probe towards leading edge of reactive foil for 80 µm rms

A mesh sensitivity study for the 80 µm case was conducted for meshes varying from 10 to 26.67 µm edge length in the z-direction and 100–1000 µm edge length in the x- and y-directions. Temperature traces at a temperature probe were compared for each mesh and it was found that mesh independence was already achieved for meshes finer than 20 µm edge length in the z-direction. It was found that the problem was mesh independent in general, particularly because the heat source per unit volume is proportional to the mesh density. The main criterion to satisfy for this problem are the mesh aspect ratio and the mesh quality because these, particularly the latter, are very critical for solution stability in that highly skewed elements were found to cause numerical divergence.

The fluid domain encompassing the solid structures was 10 mm in both the x- and y- directions and 5 mm in the z-direction. This volume was chosen as a reasonable balance between significantly displacing external boundaries away from the region of interest and maintaining a reasonably sized mesh.

In Figs. 6 and 7 the main x–z and x–y plane dimensions used in the model are shown. The most significant dimension in addition to those mentioned previously is the isolation layer gap of 35 µm. The sensing volume of each temperature probe, P1–P3, was 430 × 210 × 10 µm.

The domain has both fluid and solid mesh structures, with thermal properties shown in Table 1. The material properties are compiled from the ANSYS material databases and from a material data sheet for GreenTape™ DuPont DP 951 material. The silicon, LTCC and reactive foil are assigned solid states, whereas the solder and air are assigned fluid status. The heat transfer between all these entities is catered for through a combination of the energy equation and the implementation of coupled boundary conditions on every interface (two-sided walls) between solid structures.

The melting/solidification model was activated in ANSYS Fluent, specifically for the solder, such that

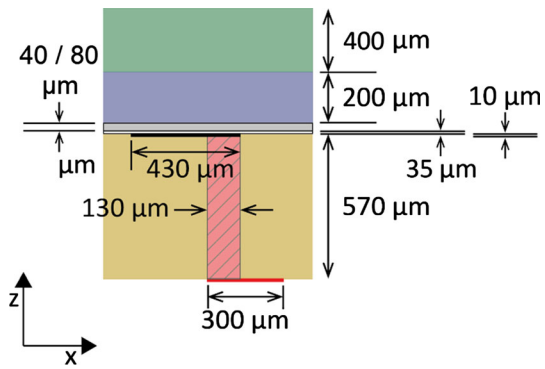

Fig. 6 Detailed dimensions in x–z plane (40 or 80 µm rms thickness depending on case studied)

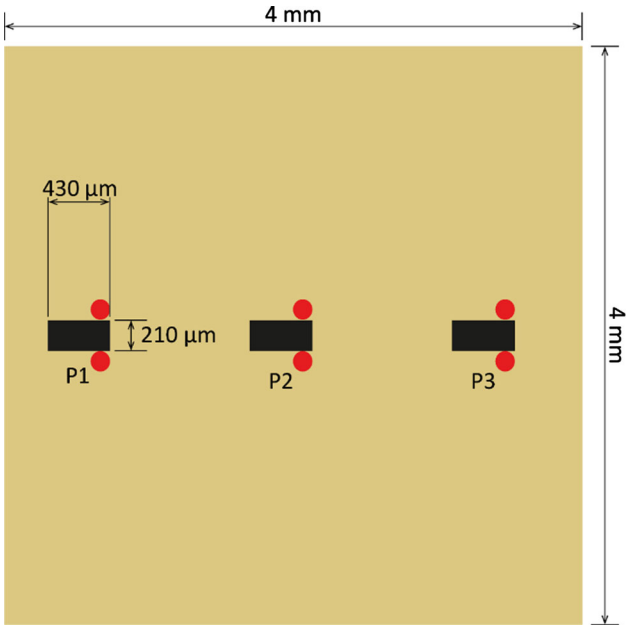

Fig. 7 Detailed dimensions in *x*–*y* plane

Table 1 Material properties

	Silicon	Green tapes	Solder	Platinum	Silver
ρ (kg/m^3)	2500	3100	7000	21,460	10,490
Cp (J/kg K)	710	600	230	132.04	234.28
K (W/m K)	100	3.3	63.2	71.538	419.97

transitions between the molten and solid state, and the associated latent heat transfer throughout, could be modelled. The pure solvent melting heat for the solder was taken to be 58.5 kJ/kg. A liquidus temperature of 217 °C and solidus temperature of 220 °C was used for the solder, corresponding to thermal properties of a SAC (tin-silver-copper) solder.

The heat released by the reactive foil was approximated through a user-defined function (UDF) in Fluent, Eq. 1, which was in essence, a one-dimensional heat source profile represented through a probability density function (PDF) propagating from the leading edge of the reactive foil, in the positive x-direction, at each time-step from the assumed point of reaction initiation at time = 0 s.

$$A \times e^{B^{(x+C-Dt)^2}} \tag{1}$$

The coefficients used for modelling the heat release were $A = 6 \times 10^{12}$ (amplitude), $B = -8 \times 10^{6}$ (PDF width) and $C = 2$ mm (to displace the reaction front to coincide with the leading edge of the shoebox model in the *x*-direction. The A and B values for the function were obtained through a trial-and-error process and possess no fundamental basis for their magnitudes. These can later be tuned and driven by experimental measurements. A reaction propagation of 1 m/s (coefficient D in Eq. 1) was chosen for the CFD simulations.

This reaction velocity is known to be a function of several factors, such as the ignition potential (Sen et al. 2017). Reactions in Al-Au nano multi-layered foils have been reported to propagate as fast as 25 m/s (Raić et al. 2011) and the range in general was quoted as 0.1–100 m/s in (Adams 2015), hence this is something which can be considered to be largely dependent on the type of foils used and 1 m/s is comfortably within this range. Furthermore, some preliminary laboratory experiments for freestanding layers have resolved propagation velocities of between 4.7 and 6 m/s for foils which will later be used for joining LTCC substrates together and or onto silicon chips. It is known that the presence of surrounding structures will supress the propagation velocity, thus making 1 m/s a reasonable choice.

Three temperature probes, made from silver vias and platinum pads, were also integrated into the model. These are to be manufactured in a way that they are integrated into the green tape structures and as close to the reactive foils as possible. These simulations allow to both to help with the understanding of the requirements for manufacturing similar physical prototypes for experimental work and to understand the extent of the interference caused by the presence of such structures. The identical temperature sensor probes are labelled P1–P3 in Fig. 7, where their leading edges are displaced by $\Delta x = 1$ mm and the upper surfaces of the probes lie 35 µm below the reactive foil. The leading tip of the P1 temperature probe is 0.72 mm displaced in the *x*-direction from the location where the reactive foil is initiated. Each Pt measuring pad has a volume of 0.0009 mm^3 and volumetrically averaged temperatures were assumed to be equivalent to what would be observed experimentally.

In ANSYS Fluent the pressure-coupled transient solver was used, together with the implicit Volume of Fluid model with 2 Eulerian phases. Furthermore, the energy equation was activated and the 2-equation k-Ω SST model was used for turbulence modelling. The melting/solidification model was used with a mushy zone parameter of 100,000. An inlet velocity of 0.1 m/s on the *y*-max boundary was used, with a corresponding zero gauge pressure boundary on the opposite *y*-min face.

On the inlet boundary a turbulence intensity of 5% and a turbulence viscosity ratio of 10 is used and, similarly, on the outlet boundary a reflow turbulence intensity of 5% and a reflow turbulence viscosity ratio of 10 was used for any reversed flow on the outlet boundary. These boundaries were used in the model such that air could be allowed to enter and leave the domain and a small inlet velocity was

found to be more stable for numerical convergence in the continuity equation than just using constant pressure boundaries. Since this inlet velocity was low, crossflow cooling effects were assumed to be negligible.

The entire velocity field for the fluid domain is initialised in the positive *y*-direction with this crossflow value of 0.1 m/s, apart for the solder region which is individually patched with 0 m/s velocity. This crossflow ensured that reversed flow back into the domain on the outlet boundary was constrained to being present in only the initial time-steps, if at all, and allowed for convergence to be achieved in the continuity residuals below the default threshold of 10^{-3} for every time-step. The temperature field, for both fluid and solid bodies is initialised at 300 K, likewise flow through the inlet boundary, or reversed flow being re-ingested at the outlet boundary has a specified temperature of 300 K.

A fixed time-step of 10^{-6} s was used for 10,000 time-steps up to 0.01 s., The temperature data were written out to file for every time-step, with temperature and liquid fraction contours written out every 10^{-4} s. Convergence for each residual of the governing equations was achieved for every time-step. A maximum of 200 iterations per time-step was allowed to permit sufficient scope for convergence of the initial time-steps. As the solution progressed convergence after a single iteration per time-step became possible.

PISO (Pressure-Implicit with Splitting of Operators) pressure–velocity coupling was used, with 2nd order upwind schemes for all spatial discretisation and 2nd order bounded implicit for the transient formulation. The Boussinesq approximation was used to model the air buoyancy effects caused by the air temperature gradients, with a constant coefficient of thermal expansion of 0.0034/K. This approximation is used because it is typically more stable than utilising models which explicitly compute air density changes for all terms in the governing equations and not just the body forces. This means that the air density is maintained at its constant value of 1.225 kg/m^3.

3 Results

3.1 CFD simulation results for reactive multi-layer thickness of 40 µm

Here results are presented for an rms thickness of 40 µm. Figure 8 shows the temperature contours at 1 ms after the initiation of the reactive foil reaction on an *x*–*z* plane intersecting with the centres of the probes. The reaction is observed to have penetrated approximately 1 mm through the foil, hence corresponding to the anticipated reaction propagation speed of 1 m/s.

Figures 9, 10 and 11 show the temperature contours at 2, 3 and 4 ms after reaction initiation. The wave front is observed to continue its propagation from left to right throughout the reactive foil and the solder and silicon above the reactive foil are acting to effectively spread the heat released by the reactive foil.

In contrast to the effective spreading of the heat in the positive z-direction Fig. 11 shows that, despite the reactive foil reaching the point of exhaustion, there is very little heat absorbed in the green tapes which could be isolating the temperature probes and suppressing their ability to reveal insights as to what is happening live inside the reactive foils.

In Fig. 12 the temperature contours are shown after 2 ms—corresponding to the midpoint of the reaction time-span in an *x*–*y* plane bisecting the Pt pads. Here the temperature contours in the immediate proximity of the probes are slightly reduced, owing to some of the heat generated by reactive foil being conducting further along the probes and thus spreading it out faster than the LTCC. The thermal interference caused by the probes at a depth of 35 µm appears to be negligible when looking at Fig. 13 which shows the temperature contours at the interface between the rms and the isolation layer in the *x*–*y* plane. However, it must also be noted that these probes are simulated in a passive mode and additional heat source inputs from the current supplied to the thermocouples are not incorporated in the model and as such their potential significance can't be ruled out.

The graph in Fig. 14 of the volumetrically averaged temperatures at the 3 temperature probe locations shows the time–temperature history, similar as to how data would appear in an experiment. In Fig. 14 it is observed that P1 is the first probe to experience an increase in temperature, as would be expected, of approximately 75 °C to the initial peak from the initial temperature of 300 K (27 °C). P2 and P3 start their respective increases in temperature after 1.2 and 1.6 ms, P2 achieving slightly higher initial peak temperatures than seen at P1, owing to thermal conduction spreading the heat released from the reactive foil upstream, and likewise there is a slight increase in the peak temperature for P3. There is an initially fairly linear increase in temperature until the latent heat of the solder starts to become significant, whereafter the spreading of the heat slows down greatly. After approximately 7 ms, corresponding to just under 2 times the reaction duration, the temperature traces coalesce thereafter.

In Figs. 15 and 16 contour plots of the solder liquid fraction are presented after 1 and 4 ms. In both of these figures only a small bubble of solder is melted and this does not grow in size but the region of the initially melted solder bubble in Fig. 15 quickly re-solidifies by the contour plot of liquid fraction in Fig. 16.

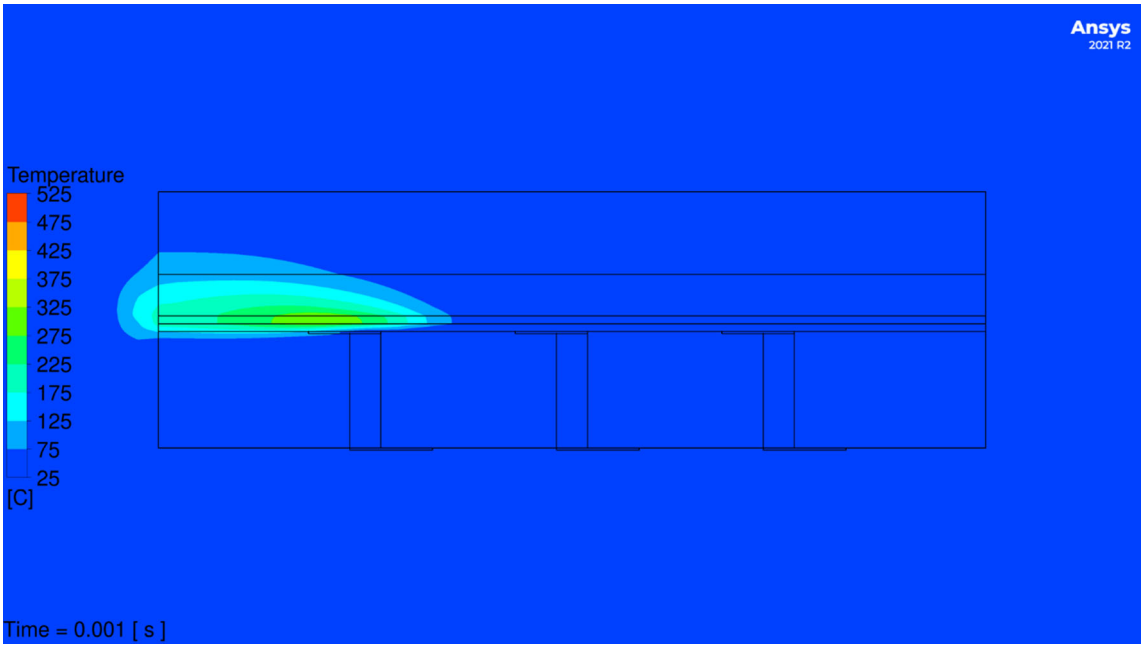

Fig. 8 Temperature contours after 1 ms, x–z plane, for 40 µm rms

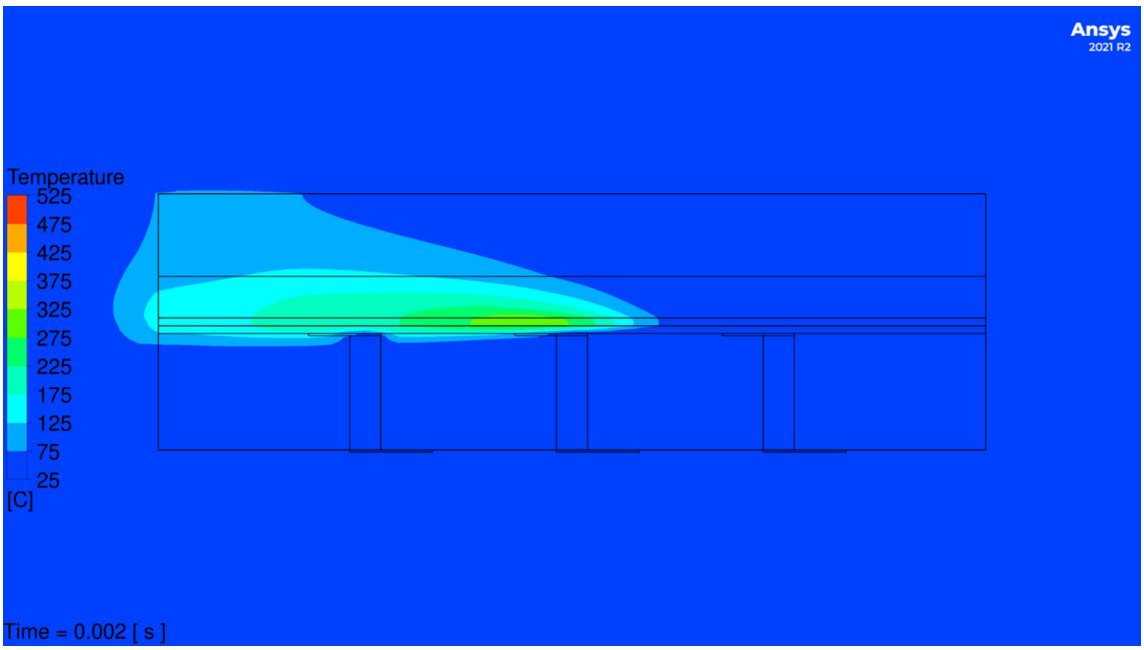

Fig. 9 Temperature contours after 2 ms, x–z plane, for 40 µm rms

In Fig. 17 the solder liquid fraction is shown for the final time-step that was calculated, namely 10 ms where all of the solder is found to have re-solidified. It can be observed that proximal to the leading and trailing edges of the reactive foil the solder still appears to be undergoing transition between it's liquid–solid state. This is due to these cells being on the solder:air interface, which despite being relatively sharp with this detailed mesh is still finite. This liquid fraction contour is in effect the same as that of the initial condition at time = 0 s, because all the solder has re-solidified, albeit there is no longer a uniform temperature.

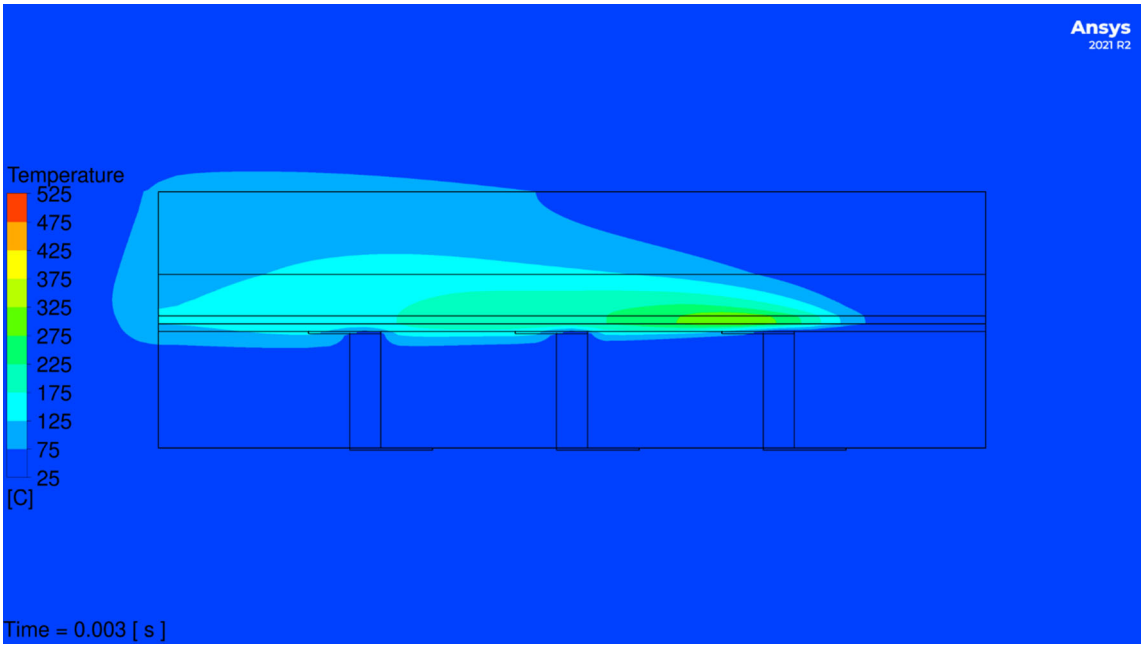

Fig. 10 Temperature contours after 3 ms x–z plane, for 40 µm rms

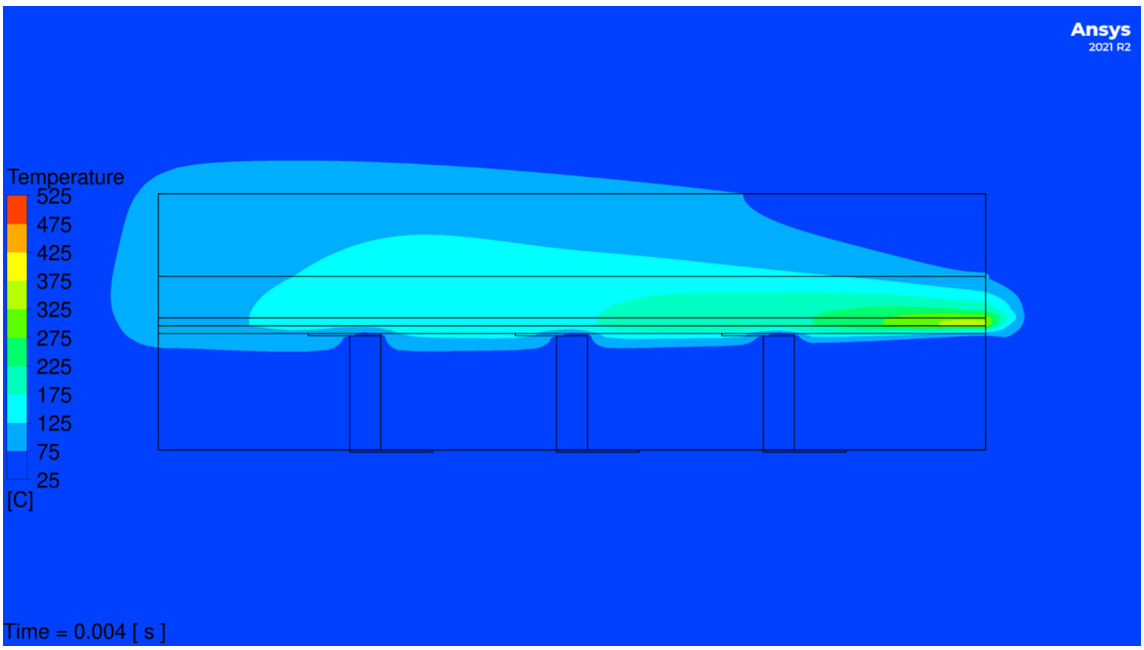

Fig. 11 Temperature contours after 4 ms x–z plane, for 40 µm rms

3.2 CFD simulation results for reactive multi-layer thickness of 80 µm

Here similar results for an rms thickness of 80 µm are presented. In Fig. 18 the temperature contours are shown 2 ms after reaction initiation. The peak temperatures are observed to be around 200 °C higher for this 80 µm thick foil than the 40 µm foil in Fig. 9 with a corresponding increase in the spreading of the heat in the solder and silicon.

A similar increase in the peak temperatures of around 200 °C is observed in Fig. 19 and by this point the spreading of the heat is much more significant, when making comparisons to Fig. 11. It can also be observed that penetration of the heat in the first via for the first probe (P1)

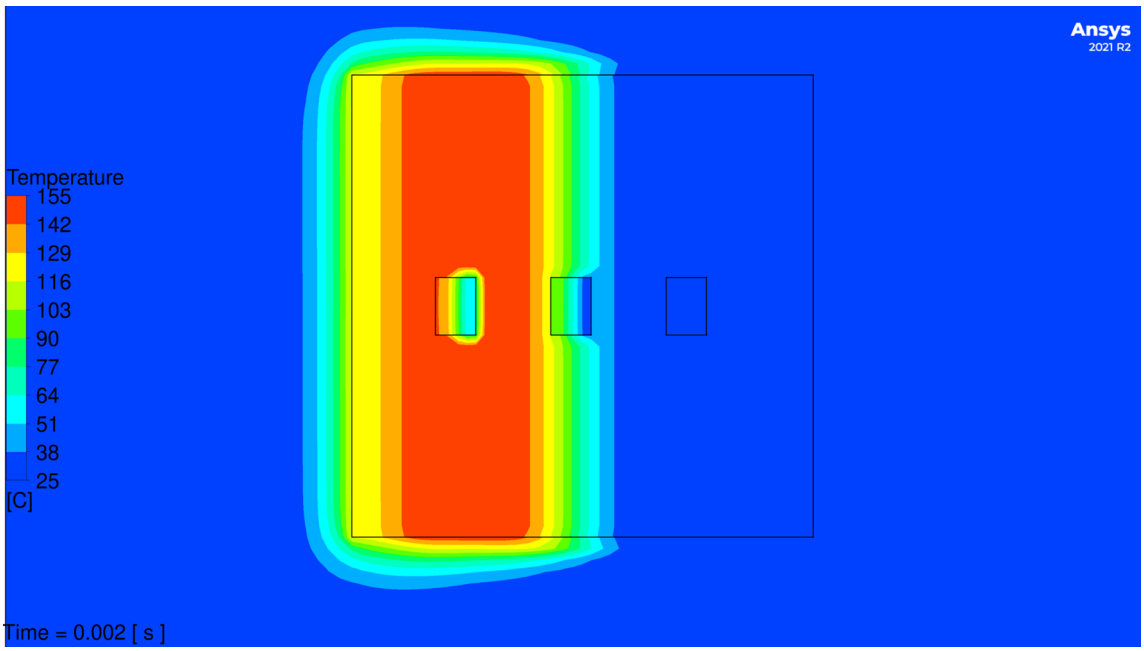

Fig. 12 Temperature contours on *x*–*y* plane bisecting probes after 2 ms, for 40 µm rms

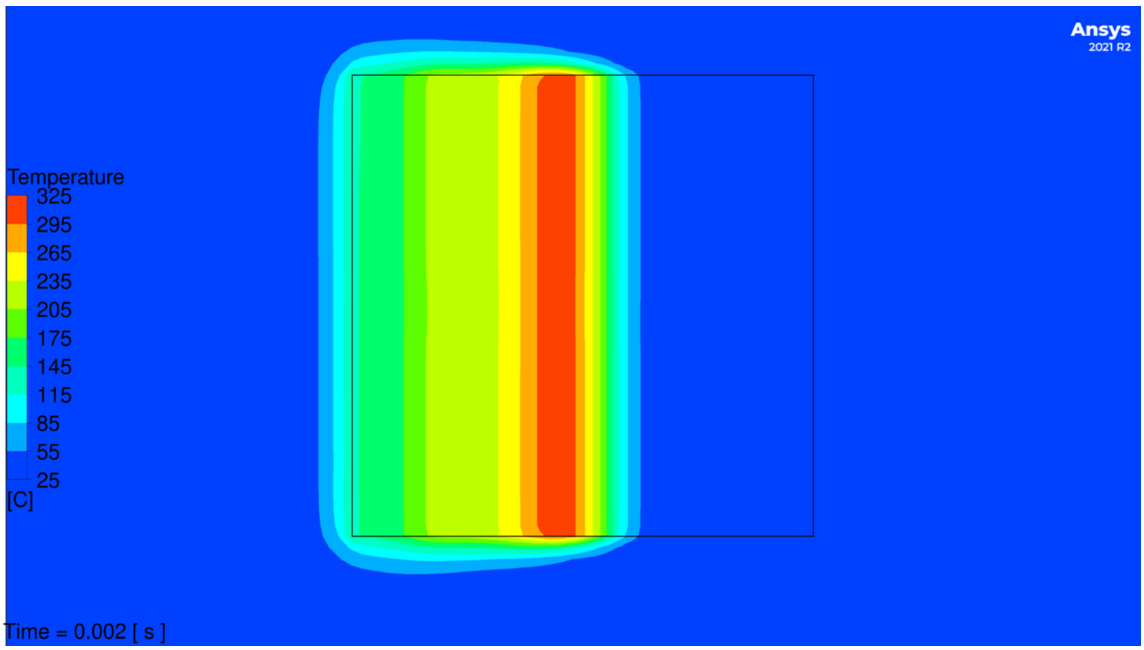

Fig. 13 Temperature contours on *x*–*y* plane at interface between rms and isolation layer after 2 ms, for 40 µm rms

has begun at this stage although was yet to occur in the 40 µm case.

In Fig. 20 a temperature contour plot is shown for the final time step, corresponding to a solution time of 0.01 s. Here one can see that the heat has become well spread around the solder and the silicon but the penetration in the LTCC is still limited, owing to its unfavourable thermal properties for conducting heat.

In Figs. 21, 22, 23, 24 and 25 the solder liquid fraction contours are shown for 1, 2, 3, 4 and 8 ms for the 80 µm thick rms. It is observed that the amount of solder that is melted by the rms is much more significant than for the 40 µm case. In Fig. 21 a molten solder bubble forms at the leading edge and this grows in Fig. 22 to a much larger extent in not only the direction of the reaction but also normal to it. In Fig. 23 the initially molten region after

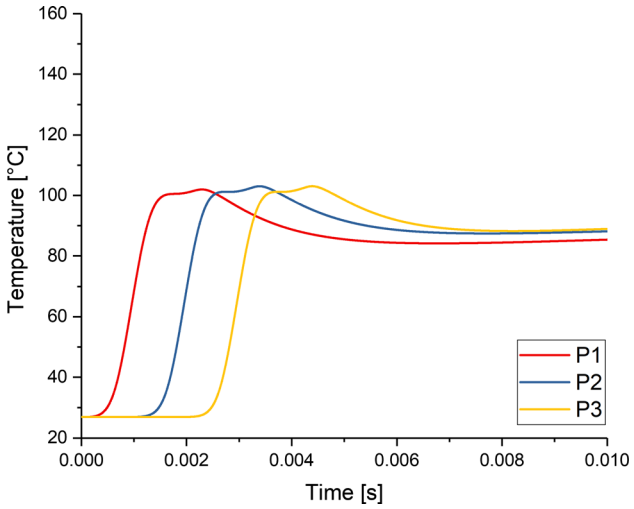

Fig. 14 Volumetrically averaged temperature probes P1–P3 vs. time, for 40 μm rms

1 ms starts to re-solidify and the molten region of solder reaches its maximal extent. After 4 ms (Fig. 24) there is now a fully re-solidified region at the site of reaction initiation, and it is clear by this stage that even this very thick foil thickness would be insufficient to melt such a large quantity of solder.

In Fig. 25 the liquid fraction solder contours are shown after 8 ms from reaction initiation. Here it can be seen that the re-solidification of the solder is almost complete. There are however some interesting details to observe. Due to the presence of the vias and the probes removing heat there appears to be two small, localised regions above the probes which re-solidify at a faster rate. This localised variation in the re-solidification can also be seen in Fig. 24 for the first probe.

In Fig. 26 the volumetrically averaged temperatures for the three temperature probes, P1–P3 are shown. In this graph three distinct peaks that occur approximately after 1.8, 2.8 and 3.8 ms are observed. Given a pitch between the probes of 1 mm, this would correspond to a reaction speed of 1 m/s. Therefore, it could be said with some confidence, that an array of thermocouples embedded in green tape substrates displaced 35 μm from the reactive foil should be capable of experimentally determining a reaction speed in

Fig. 15 Solder liquid fraction after 1 ms, for 40 μm rms

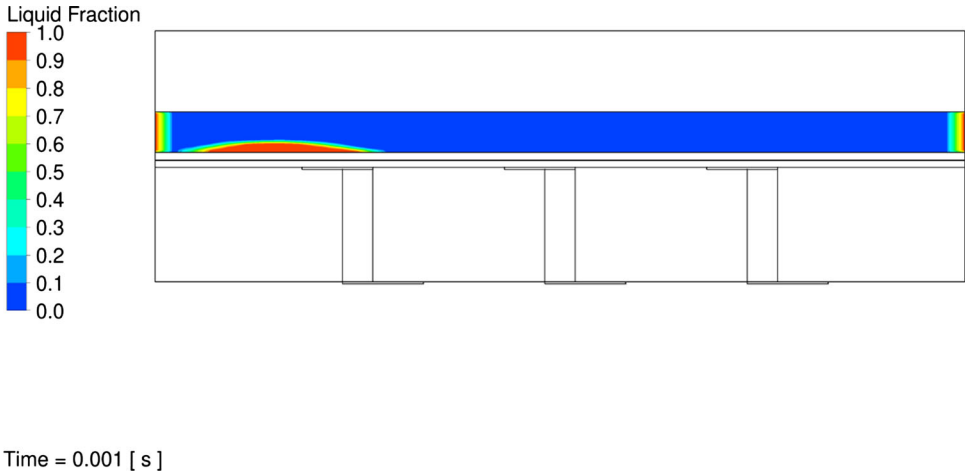

Fig. 16 Solder liquid fraction after 4 ms, for 40 μm rms

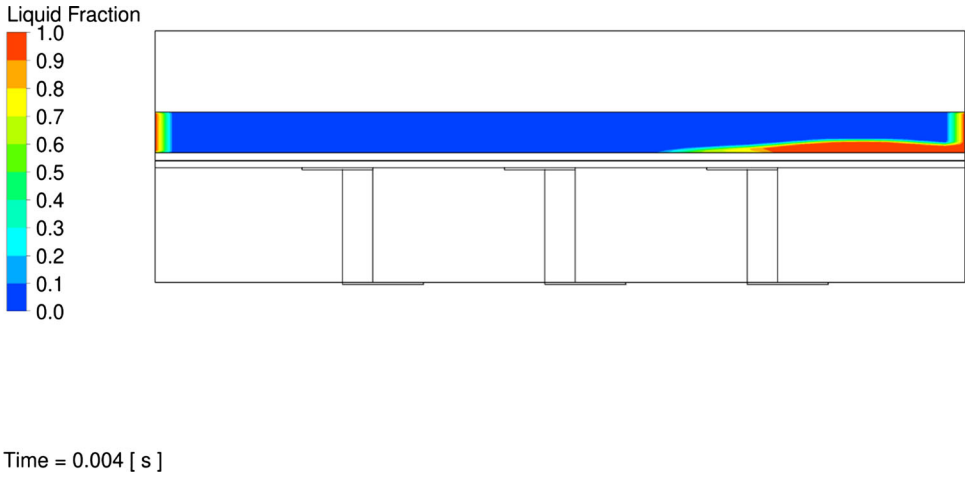

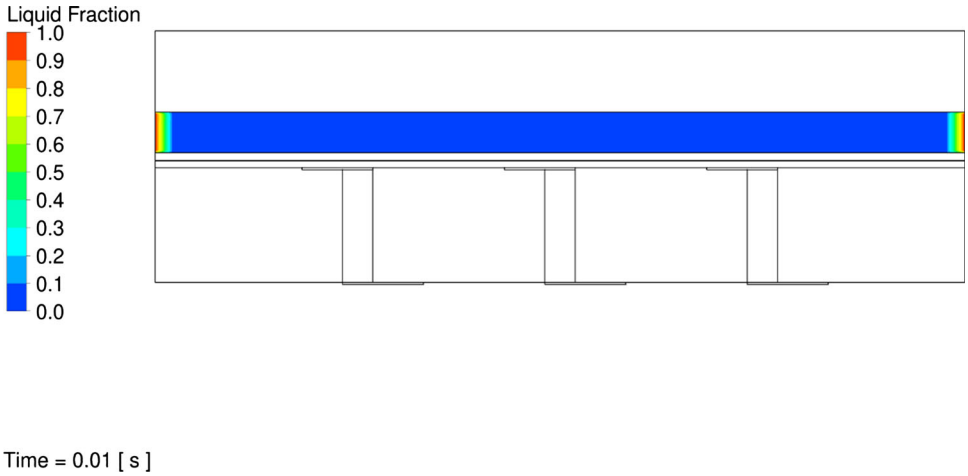

Fig. 17 Solder liquid fraction after 10 ms, for 40 µm rms

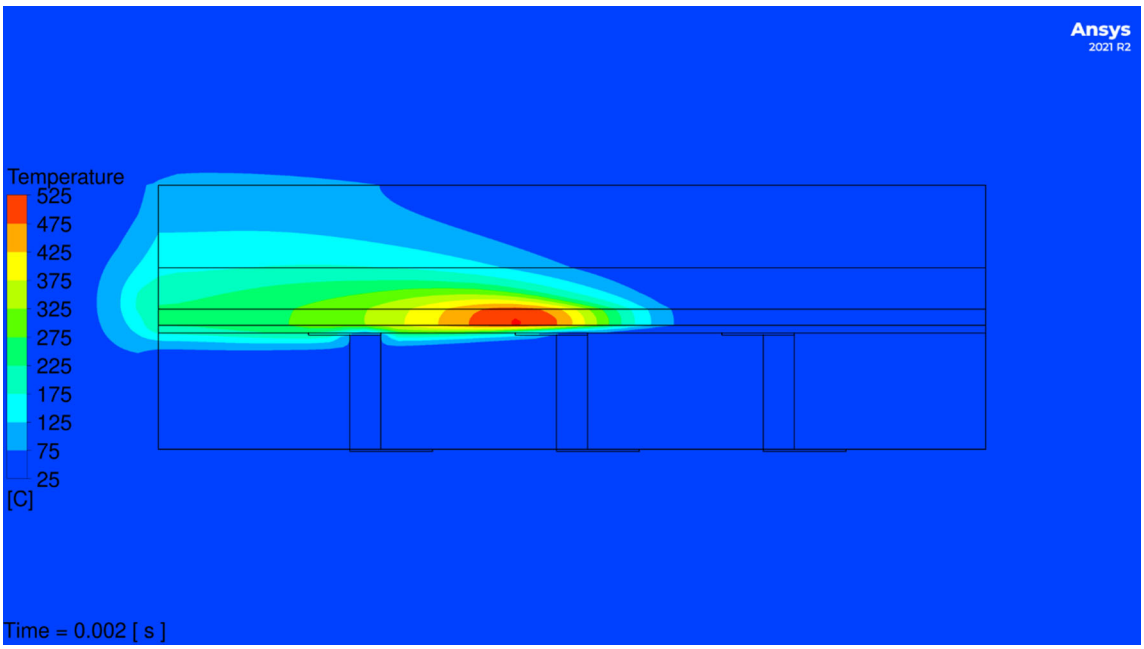

Fig. 18 Temperature contours after 2 ms, x–z plane, for 80 µm rms

this range. This would be subject to such an isolation layer thickness being realisable, in terms of manufacturing, and having adequate frequency response, synchronisation, sampling frequency etc. from the temperature recording equipment.

4 Discussion

The simulations demonstrate that it is possible to obtain the time-history of temperature contours throughout these structures, which are to be bonded through reactive multi-layers by using strategically placed temperature sensors isolated by a 35 µm thick isolation layer. Owing to the ability to track the melting and solidification of solder, CFD can be used effectively to assess the number of layers required/total reactive foil thickness to form a functioning solder joint between components and this offers a crucial insight into manufacturing requirements. Furthermore, by using the computed thermal loads as inputs in mechanical models, the mechanical influence on surrounding components could be assessed such as to optimise the balance between achieving a successful bond and minimising the thermomechanical impact incurred elsewhere.

It was interesting to compare the two cases of 40 and 80 µm reactive foils in terms of their temperature traces and in the case where the majority of the solder remained unmelted – 40 µm, the peaks on the temperature measurements were not as discernible as they are for the 80 µm thick foil where the temperature rises well beyond the

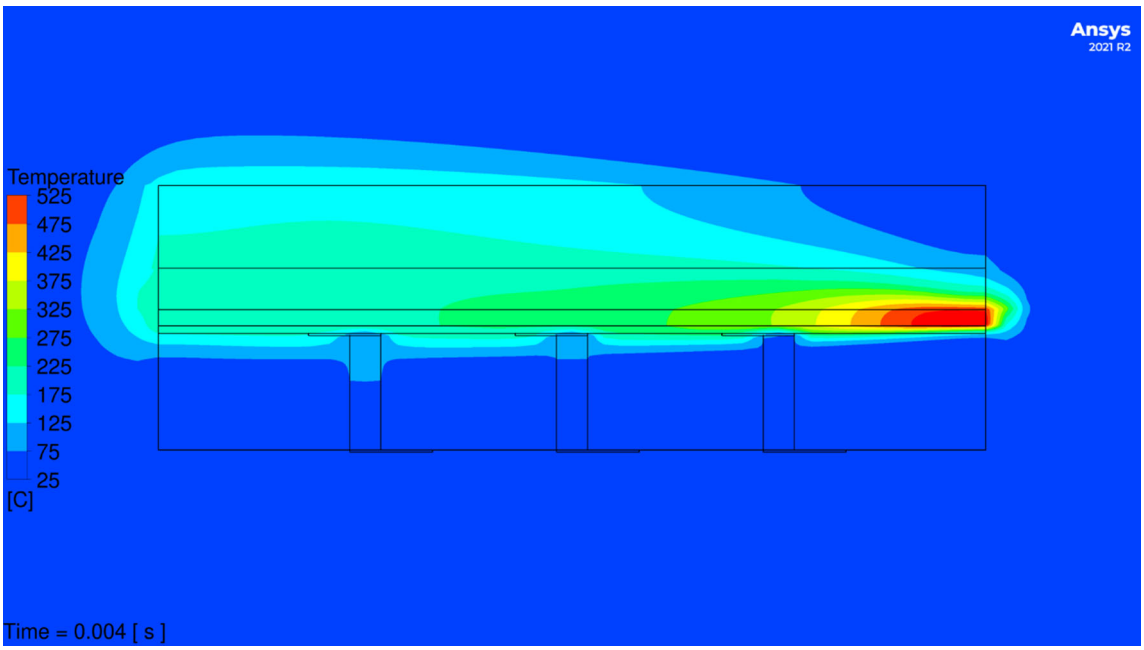

Fig. 19 Temperature contours after 4 ms, x–z plane, for 80 μm rms

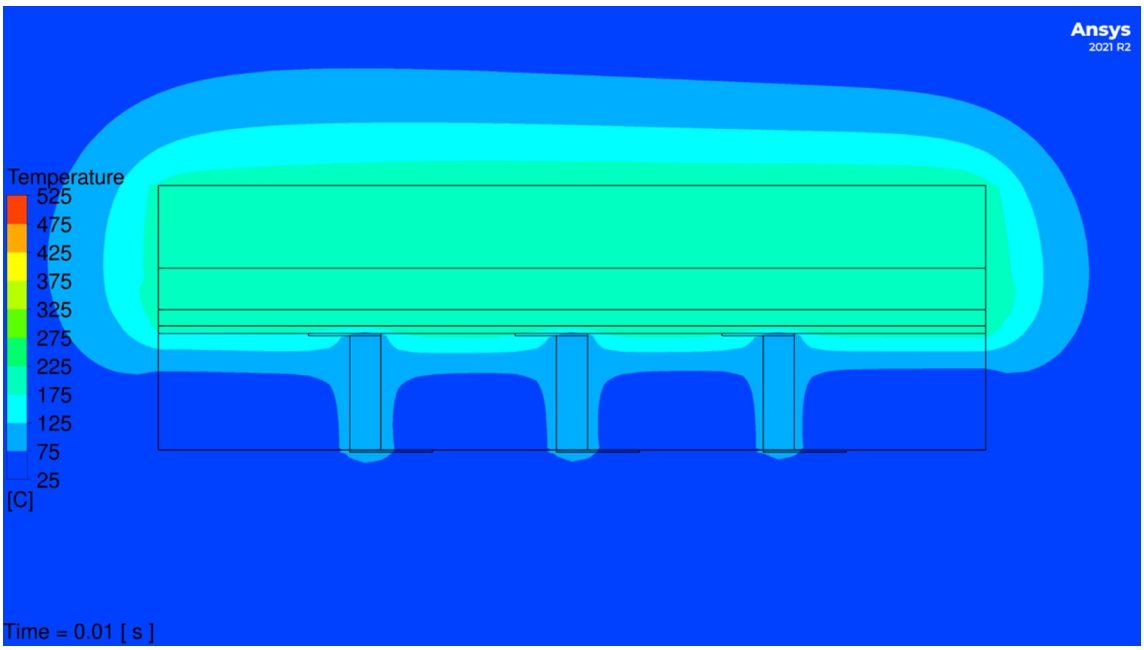

Fig. 20 Temperature contours after 10 ms, x–z plane, for 80 μm rms

solder latent heat region and the peaks can be clearly recorded. Thus, it can be concluded that it will be more difficult to resolve the reaction speed using a temperature array in cases where the solder temperatures don't go significantly above the melting point of the solder.

Although it is said to be relatively straight-forward to measure the burning rates of reactive foils, due to the intense luminescence of the wave front, temperature measurements are more complicated because of the interference caused by the thermocouples. The thermocouples typically provide underestimated values of temperature due to their propensity to remove heat and interfere with the combustion process (Rogachev and Mukasyan 2010). The results shown here may suggest that it is more the chemical interference than the thermal interference of the probes which plays the greater role in inhibiting the reaction.

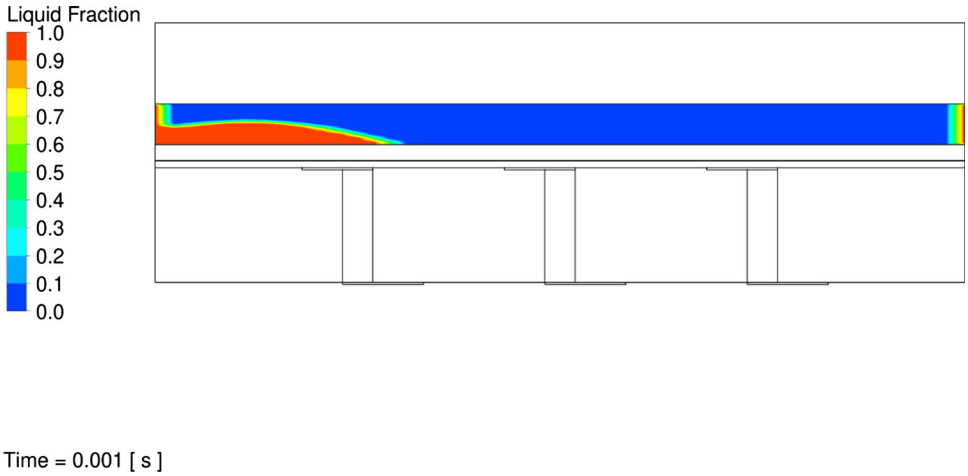

Fig. 21 Solder liquid fraction after 1 ms, for 80 μm rms

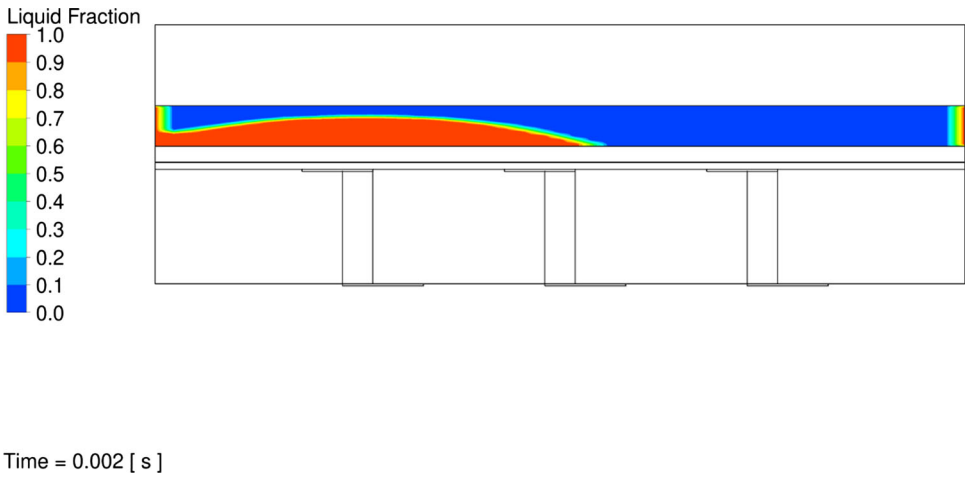

Fig. 22 Solder liquid fraction after 2 ms, for 80 μm rms

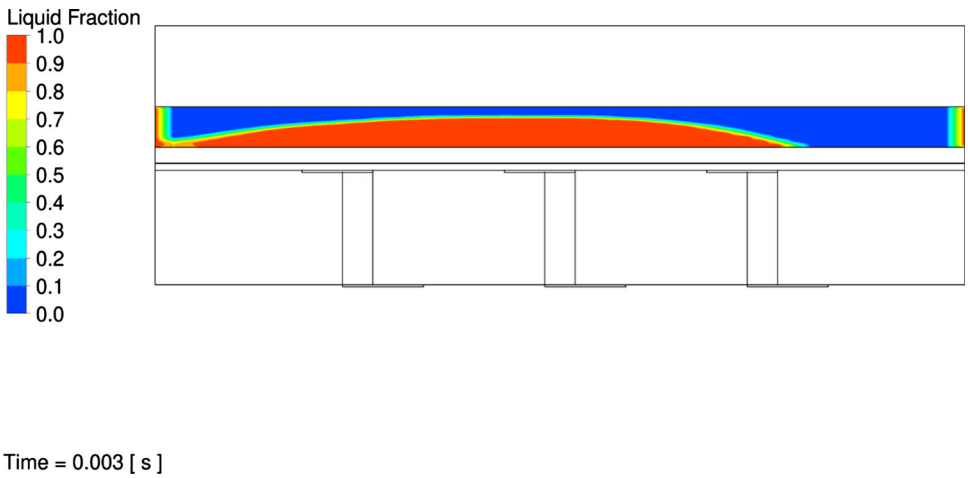

Fig. 23 Solder liquid fraction after 3 ms, for 80 μm rms

It is hoped in the future that thermocouples can be experimentally embedded in substrates very close to deposited reactive foils, without overly interfering in the reaction, to see if a good match between CFD and laboratory experiments can be obtained. Owing to these known interfering factors the thermocouples it is best to integrate the thermocouples into the CFD models, but any chemical suppression of the reaction caused by the presence of the probes is not possible to capture with the simulation method currently presented. On the other hand, surface roughness is something, which is also known to affect the reaction

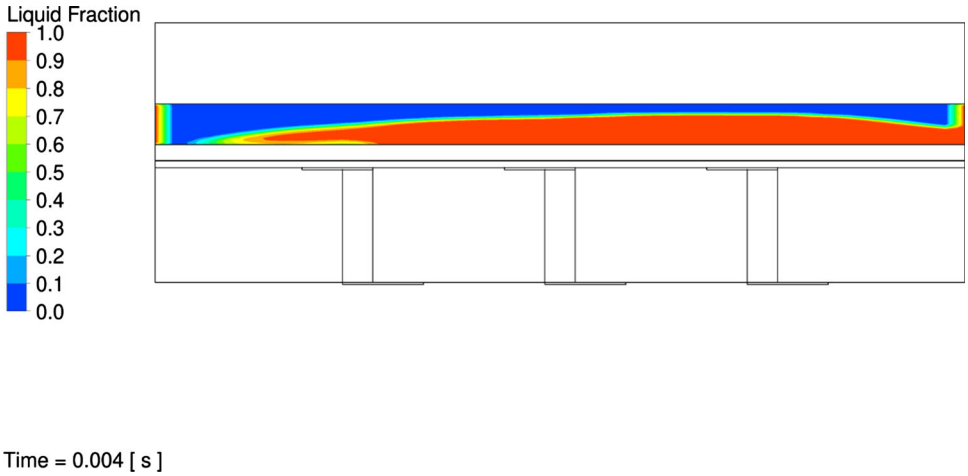

Fig. 24 Solder liquid fraction after 4 ms, for 80 µm rms

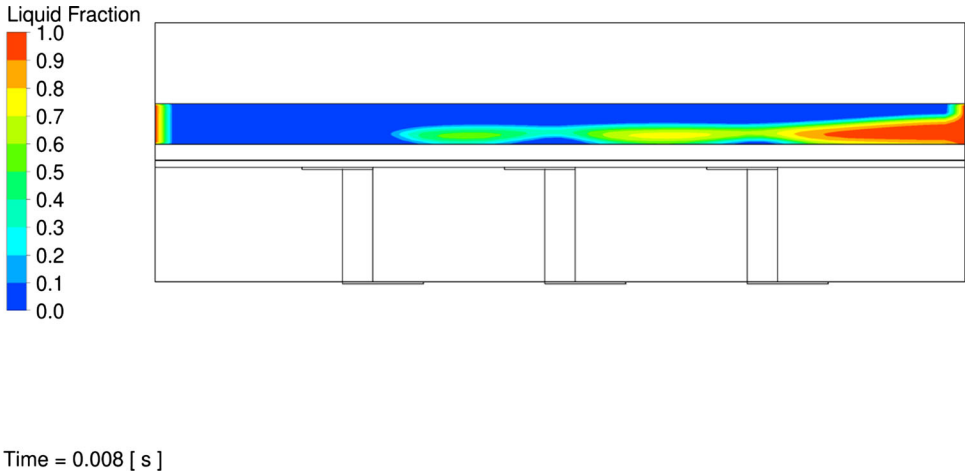

Fig. 25 Solder liquid fraction after 8 ms, for 80 µm rms

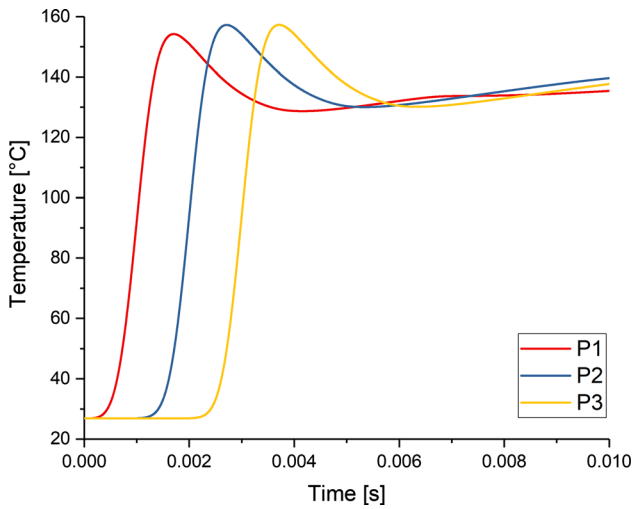

Fig. 26 Volumetrically averaged temperature for temperature probes P1–P3 vs. time, for 80 µm rms

speed, and this could potentially be incorporated into the heat release function, so there is still scope for model development.

In this research very thick solder pastes have been modelled to provide good resolution throughout the solder thickness and to obtain better insights into the behaviour than could be seen in a thinner layer with the same mesh edge length throughout the thickness. In order to achieve a complete melting of the solder there are many options available, most of which are possible to incorporate into this CFD approach. A much thinner solder thickness could of course be used in practice and, if not, then pre-heating can also be implemented. These options are available for consideration to both the manufacturer as well as this CFD simulation approach.

5 Conclusions

Using ANSYS Fluent CFD software two different reactive foil thicknesses of 40 and 80 µm used to bond a silicon chip to an LTCC substrate have been studied and it has been shown that it is possible to simulate the temperature of the bonding zone before and after the reaction. The

40 μm rms propagating at 1 m/s was only able to melt a very small proportion of the total solder thickness and this would make it difficult to track the reaction speed using Pt-100 temperature sensors embedded in the LTCC because the latent heat effects of the solder dominate the time–temperature traces.

On the other hand, the 80 μm rms was able to melt a much more significant amount of solder, approximately up to 100 μm, and in this case it would be relatively straight forward to determine the reaction propagation speed with temperature probes embedded in the LTCC substrate. Given that even this large foil was unable to melt all the solder, one of the following changes would need to be implemented. Either a thinner solder thickness or pre-heating of the to be bonded structures would need to be used. The latter option goes somewhat against one of the main attractions of using reactive foils because it would incur the mechanical penalties that their use is attempting to circumvent.

It has also been shown, based on the CFD simulations, that although the insulating effect of the LTCC substrates can potentially obfuscate temperature measurements of thermocouples embedded in the ceramic tapes, it would be possible to determine reaction speeds from assessing the displacement between peaks on temperature probe traces. This is contingent upon the effects of heating the temperature probes being negligible in a real-world scenario because this influence, and that of any chemical influence on the reaction propagation, are not included in the CFD model.

Using this CFD approach assessments can be made regarding the total reactive multilayer thickness required to melt a given quantity of solder in order to achieve an effective bond. This information can then be used to decide optimal foil properties for achieving successful soldering for selective bonding using reactive-multi-layer-systems on LTCC substrates.

Acknowledgements This work was supported by the Deutsche Forschungsgemeinschaft (DFG, German Research Foundation) – Project-ID 426204742.

Funding Open Access funding enabled and organized by Projekt DEAL.

References

Adams DP (2015) Reactive multilayers fabricated by vapor deposition: a critical review. Thin Solid Films 576:98–128

Aliouane S, Kouki AB, Aigner R (2011) Very high-Q solenoid RF inductors for SiP LTCC integration. In: 2011 IEEE MTT-S international microwave symposium. IEEE, pp 1–4

Bittner A, Schmid U (2009) The porosification of fired LTCC substrates by applying a wet chemical etching procedure. J Eur Ceram Soc 29(1):99–104

Bittner A, Ababneh A, Seidel H, Schmid U (2010) Influence of the crystal orientation on the electrical properties of AlN thin films on LTCC substrates. Appl Surf Sci 257(3):1088–1091

Braeuer J, Besser J, Wiemer M, Gessner T (2012) A novel technique for MEMS packaging: reactive bonding with integrated material systems. Sens Actuators, A 188:212–219

Ciobanu R, Schreiner C, Drug V, Schreiner T, Antal D (2015) Sensors in LTCC-technology with embedded microfluidic features, for medical applications. In: 2015 IEEE international symposium on medical measurements and applications (MeMeA) proceedings. IEEE, pp 407–410

Fournier Y (2010) 3D structuration techniques of LTCC for microsystems applications. EPFL

Golonka L, Bembnowicz P, Jurkow D, Malecha K, Roguszczak H, Tadaszak R (2011) Low temperature co-fired ceramics (LTCC) microsystems. Opt Appl 41(2):383–388

Grieseler R, Welker T, Müller J, Schaaf P (2012) Bonding of low temperature co-fired ceramics to copper and to ceramic blocks by reactive aluminum/nickel multilayers. Physica Status Solidi (a) 209(3):512–518

He S, Huang Z, Wang D, Chen Y (2014) A LTCC-BGA multi-chip packaging technology for MMICs up to Ku-Band. In: 2014 15th international conference on electronic packaging technology. IEEE, pp 138–140

Jantunen H, Kangasvieri T, Vähäkangas J, Leppävuori S (2003) Design aspects of microwave components with LTCC technique. J Eur Ceram Soc 23(14):2541–2548

Jia S, Miao M, Fang R, Guo S, Hu D, Jin Y (2012) A 3D microchannel cooling system embedded in LTCC packaging substrate. In: 2012 7th IEEE international conference on nano/micro engineered and molecular systems (NEMS). IEEE, pp 649–52

Kangasvieri T, Halme J, Vähäkangas J, Lahti M (2008) Low-loss and broadband BGA package transition for LTCC-SiP applications. Microw Opt Technol Lett 50(4):1036–1040

Lee YC, Park CS (2016) LTCC-based monolithic system-in-package (SiP) module for millimeter-wave applications. Int J RF Microwave Comput Aided Eng 26(9):803–811

Lee CK, Ahn JK, Lee CR, Kim D, Baek BJ (2013) Thermal analysis of LED lamp with LTCC-COB package. Microelectron Int

Li Y, Zeng Y, Dong D, Wang H, Tan J, Zhang J (2018) Reliability improvement of CBGA solder ball joint in LTCC-based SiP module. In: 2018 19th international conference on electronic packaging technology (ICEPT). IEEE, pp 656–661

Matters-Kammerer M, Mackens U, Reimann K, Rainer Pietig D, Hennings B, Schreinemacher R, Mauczok SG, Martiny C (2006) Material properties and RF applications of high k and ferrite LTCC ceramics. Microelectron Reliab 46(1):134–143

Park J, Albert CW, Lu KM, Chua LL, Wai JL, Kim J (2006) Double-stacked EBG structure for wideband suppression of simultaneous

switching noise in LTCC-based SiP applications. IEEE Microwave Wirel Compon Lett 16(9):481–483

Patterson FK, Gantzhorn JE, Daly TP, Rellick JR, Iwabuchi M, Kawasaki S (1989) Tape on substrate, a new systems approach for manufacturing multilayer hybrid circuits. In: Proceedings. Japan IEMT symposium, sixth IEEE/CHMT international electronic manufacturing technology symposium. IEEE, pp 147–151

Raić K, Rudolf R, Ternik P, Žunič Z, Lazić V, Stamenković D, Tanasković T, Anžel I (2011) CFD analysis of exothermic reactions in Al-Au nano multi-layered foils. Materiali in Tehnologije 45(4):335–338

Rogachev AS (2008) Exothermic reaction waves in multilayer nanofilms. Russ Chem Rev 77(1):21

Rogachev AS, Mukasyan AS (2010) Combustion of heterogeneous nanostructural systems. Combustion, Explosion, Shock Waves 46(3):243–266

Sen S, Lake M, Kroppen N, Farber P, Wilden J, Schaaf P (2017) Self-propagating exothermic reaction analysis in Ti/Al reactive films using experiments and computational fluid dynamics simulation. Appl Surf Sci 396:1490–1498

Seok S, Kim J, Lahti M (2014) A study on the effect of wire bonding interconnects of BCB capped CPW to CPW on LTCC substrate. Microw Opt Technol Lett 56(6):1378–1381

Thelemann T, Fischer M, Groß A, Müller J (2007) LTCC-based fluidic components for chemical applications. J Microelectron Electron Packag 4(4):167–172

Wilde J (2009) B4. 1-trends in assembly and packaging of sensors. In: Proceedings SENSOR 2009, vol I, pp 205–210

Wörhoff K, Prak A, Postma F, Leinse A, Wu K, Peters TJ, Tichem M, Amaning-Appiah B, Renukappa V, Vollrath G (2016) Photonic hybrid assembly through flexible waveguides. In: Silicon photonics and photonic integrated circuits V, vol 9891. International Society for Optics and Photonics, 98911pp

Yuile A, Wiese S (2020) cfd simulations of reactive multi-layer usage in joining processes. In: 2020 21st international conference on thermal, mechanical and multi-physics simulation and experiments in microelectronics and microsystems (EuroSimE). IEEE, pp 1–5

Yuile A, Schulz A, Wiss E, Müller J, Wiese S (2022) The simulated effect of adding solder layers on reactive multilayer films used for joining processes. Appl Sci 12(5):2397

Zeng Y, Li Y, Wang H, Dong D (2018) Research on the influence of dimpled ceramic SMD on mechanical strength of solder joint in LTCC-based BGA packages. In: 2018 19th international conference on electronic packaging technology (ICEPT). IEEE, pp 879–882